Journal of Fluids and Structures 59 (2015) 22–36

Contents lists available at ScienceDirect

Journal of Fluids and Structures

journal homepage: www.elsevier.com/locate/jfs

Numerical investigation of steady suction control of flow around a circular cylinder

Wen-Li Chen [a,b,c,*], Yong Cao [b], Hui Li [a,b], Hui Hu [c]

[a] Key Lab of Structures Dynamic Behavior and Control (Harbin Institute of Technology), Ministry of Education, Harbin, Heilongjiang 150090, China
[b] School of Civil Engineering, Harbin Institute of Technology, Harbin, Heilongjiang 150090, China
[c] Department of Aerospace Engineering, Iowa State University, Ames, Iowa 50011, USA

ARTICLE INFO

Article history:
Received 24 December 2014
Accepted 1 September 2015
Available online 29 September 2015

Keywords:
Circular cylinder
Suction flow control
Aerodynamic force
Vortex shedding
Three-dimensional effect
Numerical investigation

ABSTRACT

This paper numerically investigates the effectiveness of the control of steady suction on a stationary circular cylinder with several isolated suction holes on the surface at a sub-critical Reynolds number. The control effectiveness as a function of the azimuthal position, spanwise spacing and suction flow rate of the suction holes on the control of the aerodynamic forces on the cylinder and the suppression of alternate vortex shedding are taken into account. The study of the azimuthal location of the suction holes indicates that azimuthal angles of $\theta=90^\circ$ and 270°, which are close to the separation point, provide the most substantial decreases in the aerodynamic forces. When restricted to the most effective azimuthal angle, a remarkable control effectiveness can be achieved when the axial spacing between two neighboring suction holes is less than a minimum value even under a small suction momentum coefficient. However, if the axial spacing exceeds the minimum spacing, the control effectiveness will not be saturated even under a very large suction momentum coefficient. Thus, the cause of the effective aerodynamic force control is suggested to be a result of obvious three-dimensional phenomenon in the near wake, which is characterized by the generation of a convergent flow between two neighboring suction hole sections and a stronger, larger three-dimensional vortex pair adjacent to the convergent flow. It has been suggested that this strongly three-dimensional flow pattern is induced by the strong interaction between two neighboring but counter-rotating three-dimensional vortices separately produced by two neighboring suction holes. Moreover, the effects of such three-dimensional flow patterns are investigated in detail based on variations in the flow field and sectional aerodynamic forces in different cross sections. Finally, the upper limit of the axial spacing between two neighboring suction holes to form such a three-dimensional flow pattern is suggested to be between 0.75 D and 1.5 D when the suction flow rate exceeds a certain value.

1. Introduction

The flow around a circular cylinder has always been important for researchers and engineers because of its widespread practical applications (e.g., offshore risers, bridge piers, towers and cables). In the civil engineering field, inclined cables are

* Corresponding author.

http://dx.doi.org/10.1016/j.jfluidstructs.2015.09.002
0889-9746/

key components of long-span bridges that are prone to wind-induced vibration or aerodynamic instability due to the low stiffness and damping rate. Thus, flow control around a circular cylinder is of great significance.

Flow control methods can be divided into two general types: passive and active flow control. The introduction of a splitter plate (aligned with the oncoming flow) downstream of a bluff body is one widely used passive control method (Roshko, 1993; Bearman and Branković, 2004). Owen et al. (2001) attached hemispherical humps to circular cylinders to control the fluctuating amplitudes of the vortex-induced vibrations of cable models.

Active flow control approaches include forced rotary oscillation, moving-wall, blowing and suction flow control. Tokumaru and Dimotakis (1991) examined the control efficacy of the sinusoidal oscillatory cylinder rotation for actively controlling the cylinder wake in their experimental study. A significant drag reduction of 80% was achieved at the Reynolds number (Re) of 15 000 for the optimal frequency and amplitude parameters of the rotary oscillation. Shiels and Leonard (2001) conducted a numerical simulation to explore the same flow control method, but with a larger range of Reynolds numbers (i.e., from 150 to 15 000). They confirmed the experimental observations at Re=15 000 by Tokumara and Dimotakis (1991) and further suggested that higher control effectiveness of drag could be obtained at higher Reynolds numbers. Wu et al. (2007) employed a flexible surface on the downstream half of the circular cylinder to generate a traveling wave when Re=500. This moving-wall control method successfully impeded the flow separation near the wall even under a strong adverse pressure gradient and eliminated the vortex shedding in the wake. Amitay et al. (1998) and Glezer and Amitay (2002) investigated the interactions of synthetic jets with cross-flows. The overall flow configurations around bluff bodies were modified dramatically by the formation of synthetic flow recirculation regions near the locations of the synthetic jets. While synthetic jets were usually placed near the separation points for flow control, Feng et al. (2010) and Feng and Wang (2012) applied synthetic jets in the rear stagnation points of circular cylinders and temporally alternated suction and blowing of synthetic jests. By increasing the suction duty cycle factor (defined as the ratio of the time duration of the suction cycle to the blowing cycle), a flow separation delay and drag reduction by up to 29% were realized.

Suction flow control methods have also been applied to various flow configurations. The surface suction slot seems to be used most widely among them, e.g., to a turbulent junction flow by Seal and Smith (1999), a wall-mounted hump by Greenblatt et al. (2006), an airfoil at transonic speeds by Qin et al. (1998) and Chng et al. (2009). Fransson et al. (2004) studied the flow field around a smooth, porous cylinder with flow suction pores uniformly distributed over its entire surface. Distinctly different from these suction methods, Chen et al. (2013a),(2013b) and Chen et al. (2014) introduced a limited number of small, isolated suction holes to manipulate vortex shedding in the wake behind a circular cylinder. Because of its steady suction, this method is called the steady suction flow control method. The method has several attractive advantages in comparison with other flow control techniques. For example, the control effectiveness of the model is considerably high (e.g., reduction of lift fluctuation by 80%). Experimental results showed that the azimuthal locations of the suction holes with respect to the oncoming airflow, the spanwise spacing between the suction holes and the suction flow rate through the suction holes have a significant effect on the wake flow characteristics, surface pressure distribution and the resultant dynamic wind loads. However, a deeper and systematic understanding of the underlying mechanism of the suction flow control is still needed, which is very useful for various practical engineering applications and further developments.

Following the experimental work of Chen et al. (2013b), (2014), the authors take advantage of more detailed information obtained by numerical simulation under the same physical conditions to further investigate the steady suction control method. Another spanwise arrangement of suction holes is also simulated. We attempt to (1) verify the applicability of the CFD technique to the suction flow control method, (2) discover the causes of the effective suction control of aerodynamic forces and vortex shedding of a circular cylinder and (3) provide further discussion on how to obtain effective control by employing this method.

2. Numerical method and validation

2.1. Governing equations

An incompressible and viscous fluid with a uniform velocity U_∞ at infinity is assumed to flow past a stationary circular cylinder. For transient flows, the incompressible ensemble-averaged governing equations (or called unsteady Reynolds averaged Navier–Stokes equations) are

$$\frac{\partial\langle u_i\rangle}{\partial x_i}=0, \tag{1}$$

$$\frac{\partial\langle u_i\rangle}{\partial t}+\langle u_j\rangle\frac{\partial\langle u_i\rangle}{\partial x_j}=-\frac{1}{\rho}\frac{\partial\langle p\rangle}{\partial x_i}+\nu\frac{\partial^2\langle u_i\rangle}{\partial x_k^2}-\frac{\partial\langle u_i'u_j'\rangle}{\partial x_j}, \tag{2}$$

The operation $\langle\ \rangle$ is ensemble averaging. The Reynolds stresses $\langle u_i'u_j'\rangle$ in Eq. (2) are modeled via the turbulent viscosity hypothesis to relate the Reynolds stress with the mean velocity gradients and eddy viscosity ν_T (see Eq. (3).

$$\langle u_i'u_j'\rangle-\frac{2}{3}k\delta_{ij}=-\nu_T\left(\frac{\partial\langle u_i\rangle}{\partial x_j}+\frac{\partial\langle u_j\rangle}{\partial x_i}\right), \tag{3}$$

2.2. Numerical method and model

The Reynolds number used in the present study ($Re \approx 3.0 \times 10^4$), which is close to that of Chen et al. (2014), is within the range where wind-induced vibrations of stay cables were observed in the field studies of Zuo et al. (2008) and Zuo & Jones (2010). All flow simulations were performed using the commercial software ANSYS CFX 14.0 (ANSYS CFX, 2011). The spatial discretization method is the finite volume method (FVM). The convection scheme and transient scheme are "high resolution" and "second order backward Euler", respectively. An unsteady RANS turbulence model based on the eddy-viscosity hypothesis was adopted, i.e., the shear stress transport (SST) turbulence model first proposed by Menter (1994). Because of space limitations, the SST governing equations and related parameters are not presented here; they can be found in Menter (1994) and Menter et al. (2003). Conceptually speaking, the SST model applies two blending functions to combine different elements of conventional turbulence models and ultimately achieves the desired features in the different regions of a complex flow. The blending functions result in a certain amount of blending of the k–ω model (Wilcox, 1988) with the k–ε model in the wake region and highly accurate predictions of the onset and amount of flow separation under adverse pressure gradients.

Fig. 1 shows the computational domain with 17 D × 6 D × 6 D (D=50.8 mm, where D is the diameter of the cylinder). The width and height are the same as the size of the wind tunnel used by Chen et al. (2014) to enable comparison between the numerical and experimental results, unfortunately resulting in a relatively small aspect ratio (L/D=6) and high blockage ratio (B=16.7%). The effects of the end walls on the flow characteristics in the central region of the test model are believed to be quite small at the Reynolds number levels of the present study, based on the findings described in Szepessy and Bearman (1992) and Norberg (1994). The boundary conditions are defined as follows: the left side is the velocity inlet with a uniform flow velocity perpendicular to the boundary of U_∞=8 m/s; the right side is set as the "outlet" with a pressure of 0 Pa relative to the reference pressure (1 atmospheric pressure); the upper, lower and side boundaries are defined as "wall" boundaries under the free slip condition; and the surface of the cylinder is set as a no-slip wall. It should be noted that the suction holes are set as velocity outlets where fluid will flow out of the region perpendicular to the cylinder's surface, which can be realized in cylindrical coordinates.

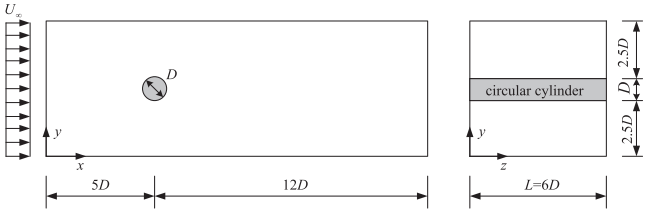

Fig. 1. The computational domain of unsteady flow around a cylinder.

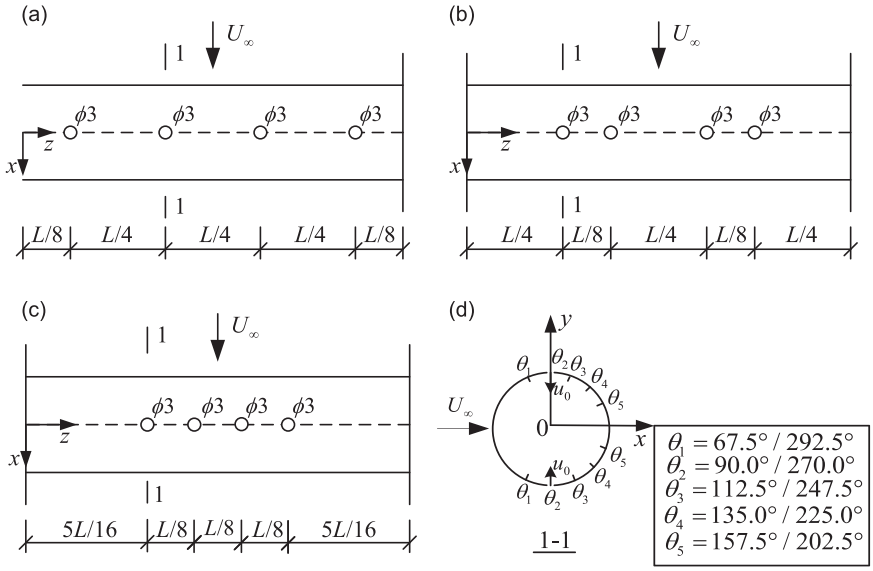

Fig. 2. Suction cases of different axial distribution modes and azimuthal positions of suction holes, citing θ_2=90° (270.0°). (a) Model 1 (L/8@L/4@L/4@L/4@L/8), (b) Model 2 (L/4@L/8@L/4@L/8@L/4), (c) Model 3 (5L/16@L/8@L/8@L/8@5L/16) and (d) Azimuthal positions of suction holes.

Three parametric variations are under consideration to study the control effectiveness of the steady suction method:

(1) The azimuthal locations of the suction holes are selected from five angles: $\theta_1=67.5^\circ$ (292.5°), $\theta_2=90.0^\circ$ (270.0°), $\theta_3=112.5^\circ$ (247.5°), $\theta_4=135.0^\circ$ (225.0°) and $\theta_5=157.5^\circ$ (202.5°). That is, each numerical model has two suction holes with the same diameter of 3.0 mm located symmetrically with respect to the oncoming flow in each crossplane. Fig. 2 uses the example of $\theta_1=90^\circ$ (270.0°) to illustrate the following three axial spacing arrangements and the possible azimuthal positions of the suction holes.
(2) The axial spacing arrangements of the small-diameter suction holes are model 1 (L/8@L/4@L/4@L/4@L/8), model 2 (L/4@L/8@L/4@L/8@L/4) and model 3 (5L/16@L/8@L/8@L/8@5L/16), where L denotes the total axial length of the cylinder.
(3) Each steady suction control is performed at one of five suction flow rates, Q=20, 40, 60, 80 and 95 L/min, where "steady" means that the suction rate remains constant in time. The suction flow rates can be converted to the corresponding flow velocity in each hole, that is, $\overline{U}_{suc}=5.89$, 11.79, 17.68, 23.58 and 28.00 m/s, respectively. Following the work of Chen et al. (2014), the suction momentum coefficient is defined as the ratio of the suction momentum flux to the oncoming free-stream momentum flux $C_\mu=2\left(\overline{U}_{suc}/U_\infty\right)^2\left(S_{suc}/DL_{ref}\right)$. Here, S_{suc} is the area of the suction holes in each suction section, and L_{ref} is the effective spacing, which is L/4 for model 1 (L/4 equally distributed), 3L/16 for model 2 (L/8 and L/4 alternately distributed) and L/8 for model 3 (L/8 equally distributed). The suction flow rate, the flow velocity and the corresponding suction momentum coefficients C_μ for each case are listed in Table 1.

The grid system is structural with an O-block surrounding the cylinder, as shown in Fig. 3. The near-wall region matches the height of the first cell near the cylinder well with $\Delta_y=0.06$ mm. In total, the grid system contains 7.0 million hexahedral elements. The detailed parameters of the grid system are shown in Table 2. The suction holes on the cylinder surface are discretized by nine elements in the circumferential direction.

2.3. Validation of the uncontrolled baseline case

The flow past an uncontrolled circular cylinder was first simulated to validate the above numerical method and model and to provide a baseline for the steady suction cases. The comparison between the present numerical results and the

Table 1
The suction flow rate and corresponding suction momentum coefficients.

Suction flow rate (L/min)		**0**	**20**	**40**	**60**	**80**	**95**
Suction flow velocity (m/s)		0	5.89	11.79	17.68	23.58	28.00
Suction momentum coefficient	Model 1 with $L_{min}=1.5$ D	0	0.0040	0.0159	0.0357	0.0635	0.0895
	Model 2 with $L_{min}=0.75$ D	0	0.0053	0.0212	0.0476	0.0846	0.1193
	Model 3 with $L_{min}=0.75$ D	0	0.0079	0.0317	0.0713	0.1269	0.1790

where L_{min} denotes the minimum spacing between two suction sections for each model.

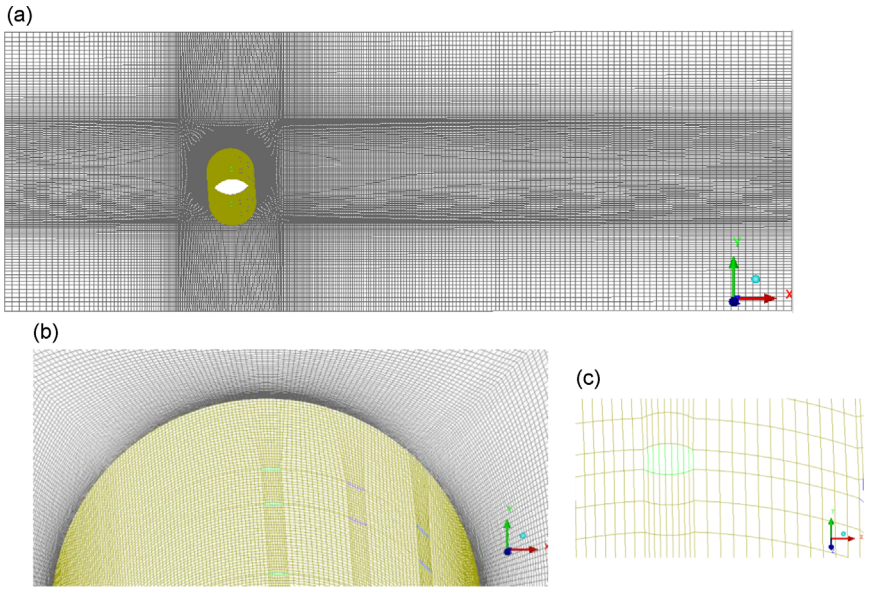

Fig. 3. Discretization of the 3D fluid region around the circular cylinder. (a) Whole mesh, (b) Close-up of the region near cylinder and (c) Close-up of a suction hole.

available experimental data under similar conditions is shown in Table 3. The blockage ratio (B), aspect ratio (L/D) and longitudinal turbulence intensity (I_u) are included. It is should be noted that the present numerical force coefficients, unless otherwise stated, were obtained based on the entire spanwise length, and the experimental force coefficients were calculated based on the sectional pressure integration. The time-averaged drag coefficient and the Strouhal number (i.e., $St = f_s D/U_\infty$) of the present numerical simulation are found to be in a good agreement with the experimental results under similar conditions. Furthermore, the present separation angle (see Table 3) and the formation length of the primary vortices in the near wake (according to the streamlines of the time-averaged velocity in Fig. 12(a)), which are very important flow characteristics for the steady suction control method, are also found to be consistent with the PIV results reported by Chen et al. (2014). The root mean square (r.m.s.) of the total lift coefficient is 0.63 in the present numerical simulation. Although the r.m.s. of the total lift coefficient was not provided explicitly in Chen et al. (2014), it could be roughly estimated by comparing the fluctuations of the velocity in the wake shown in Fig. 12(a). The turbulent kinetic energy (i.e., $T.K.E. = 0.5 \times (\overline{u'u'} + \overline{v'v'})/U_\infty^2$, where the overbar indicates time averaging) in the wake was overpredicted to a small degree in the present simulation. The reason possibly lies in the inherent limitations of URANS modeling, where the two-dimensionality of the periodic Karman vortices is possibly enhanced to some degree in the absence of sufficient perturbations from three-dimensional random turbulent motions. Because the discrepancies of the turbulent kinetic energy in the uncontrolled case are within a reasonably small range, they will not affect the objectives of the present study in general (i.e., to evaluate the effectiveness of the steady suction control method and to elucidate the underlying mechanism of the effective control). More detailed evidence will be provided in Section 4.2, and the validation of the control cases will accompany the numerical results of the steady suction control method.

Table 2
Grid parameters.

Grid parameters	
Central O-block grid	$360 \times 90 \times 103$
Total number	7.0 million
Resolution in span-wise direction	0.059 D
Height of the nearest cell to cylinder	0.0012 D
Nodes of holes in circumferential direction	10
Nodes of holes in span-wise direction	2

Table 3
Summary of the experimental results under similar conditions. The span-wise aspect ratio (L/D), blockage ratio (B) and longitudinal turbulence intensity (I_u) are also reported.

References	Re ($\times 10^4$)	L/D	B(%)	I_u(%)	C_x	St	θ_s
West and Apelt, 1982	3.0	6	15.2	≤ 0.15	1.35	0.21	–
Braza et al., 2006	6.5	4.8	20.8	1.5	1.62	0.21	–
Chen et al., 2014	3.0	6	16.7	0.8	1.24	0.21	≈ 90
Present	2.8	6	16.7	1	1.27	0.22	88

where the experimental drag coefficients C_x were based on the sectional pressure integration, while the present numerical drag was obtained based on the whole span-wise length; the separation points θ_s are estimated as the angular distance where the velocity gradient at the wall begins to change from positive to negative.

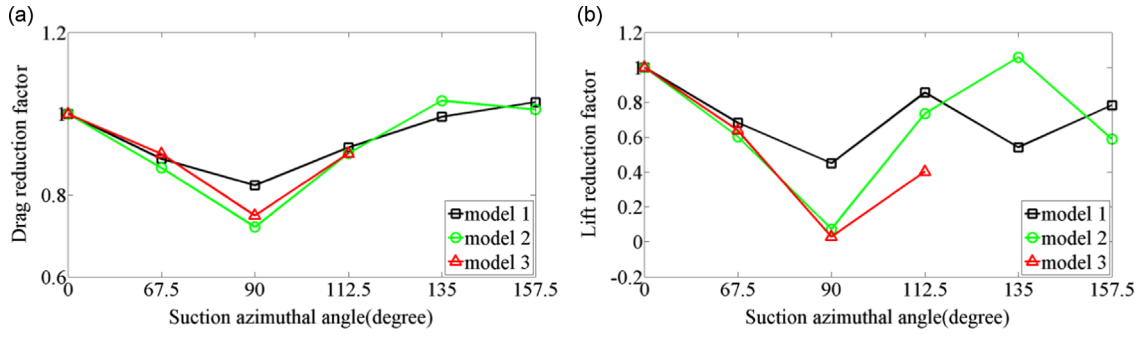

Fig. 4. Variation trend of reduction factors of (a) mean drag coefficient and (b) the fluctuation of lift coefficient against suction azimuthal angle for the same suction rate 95 L/min. Note: The simulation of model 3 is only performed for the azimuthal angle of the suction holes between 0° and 112.5°.

3. Suction control effectiveness under various suction conditions

3.1. Effect on the total aerodynamic characteristics

First, the suction rates are restricted to the maximum value tested in the present research (i.e., 95 L/min) to study the effect of the azimuthal locations of the suction holes on the control effectiveness for all three models with different axial spacing arrangements. The force reduction factor, written in the form $f=C_{x\_with\_suction\_control}/C_{x\_without\_control}$, is adopted according to Chen et al. (2014) to evaluate the control effectiveness on the time-averaged drag coefficients and r.m.s. of the lift coefficients. Fig. 4 shows the trends in the variations of the reduction factors as a function of the azimuthal angle of the suction holes. In general, the steady suction control method executes significantly better control over the fluctuation of the lift coefficient than the mean drag coefficient, regardless of the suction angle. Between 0° and 112.5°, the aerodynamic force coefficients present a coincidental trend for all three models. Quantitatively speaking, all three models have similar reduction factors when the azimuthal angle is 67.5°, which is upstream from the separation point. When the azimuthal angle is 90°, which is very close to the separation point (88°), the reduction factors decreased to the lowest level, specifically 0.72 and 0.07 for the drag and lift coefficients, respectively. Therefore, it is suggested that the suction flow control method has less effect on the aerodynamic force coefficients when the suction holes are located in front of the separation point or deep in the flow separation region. The method can achieve the greatest control when the azimuthal location of the suction holes is $\theta_2=90°$, which is very close to the separation point.

Based on the above analyzes, a suction angle of 90° (270°) is the optimal choice for steady suction flow control among all tested azimuthal positions. Thus, the suction angle is fixed at 90° (270°), and the influence of the suction flow rate and axial arrangement models on the drag and lift coefficients can then be explored, as shown in Fig. 5. It is clear that the control effectiveness over the lift coefficient is significantly larger than over the drag coefficient. In terms of the effect of axial spacing, the control effectiveness of model 2 and model 3 significantly exceed that of model 1. An increase in suction flow rate leads to a continuous decrease in force coefficients for model 1. In contrast, model 2 and model 3 present a distinct phenomenon from model 1. Specifically, the mean drag coefficient and the r.m.s. of the lift coefficient are reduced as the suction momentum coefficient increases from 0 to 0.03; however, when the suction momentum coefficient exceeds 0.03, the reduction factors from the drag and lift reach a plateau and become stable. That is, a further increase in suction strength has little or no influence on the control effectiveness after the suction flow rate exceeds a certain “threshold” value. The control effectiveness of model 2 is slightly higher than that of model 3 when C_μ is approximately 0.03 although models 2 and 3 behave generally similar. Moreover, the sectional force coefficients by Chen et al. (2014) are added in Fig. 5, where MP1 is the pressure measurement plane at the mid-span of the test model, and MP2 is in the suction hole section. The

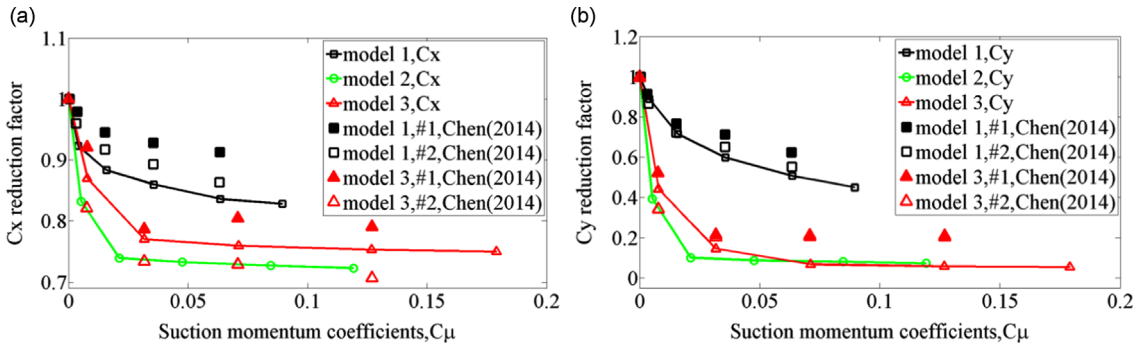

Fig. 5. Contrast of drag and lift reduction factor against suction momentum coefficients and axial spacing arrangement, with fixed 90° suction angle. In Chen et al. (2014)'s results, MP1 means the pressure measurement at the mid-span section of the test model, and MP2 is at the suction hole section.

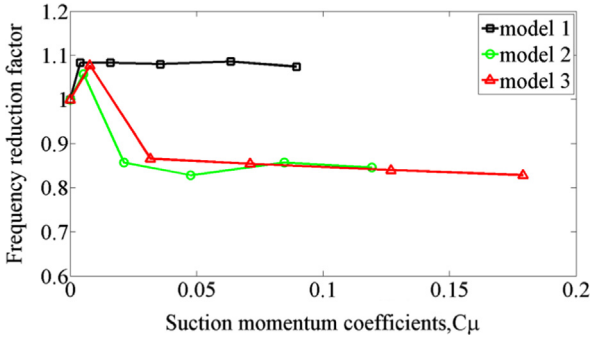

Fig. 6. Frequency reduction factor against suction momentum coefficients and axial spacing arrangement, with fixed 90° suction angle.

numerically obtained total forces and the experimental sectional forces exhibit a similar variation tendency against both the axial spacing of suction holes and the suction flow rate. For model 3, the numerical results of the total drag are intermediate between the experimental results obtained based on two cross sections, which agree with each other reasonably well. The discrepancy between the numerical and experimental lift reductions may be attributed to the limitation of the URANS turbulence model for accurately predicting the random turbulent motions, which will be discussed further in Section 4.2.

Fig. 6 shows the reduction factors of the vortex shedding frequency versus suction momentum coefficients and axial spacing arrangements under a fixed 90° (270°) suction angle. For all of the cases of model 1 and the cases with $C_\mu < 0.02$ for models 2 and 3, the frequency increases by approximately 10% relative to the baseline case. As opposed to the reduction factor of 1.1 obtained for model 1 when $C_\mu > 0.02$, the frequencies of models 2 and 3 decrease and stabilize at approximately 0.85. If roughly imagining the wake flow according to the frequency, two distinct flow types could be recognized based on the two frequency plateaus. One is true for all cases of model 1, and the cases with $C_\mu < 0.02$ for models 2 and 3 featured a higher shedding frequency, and the opposite is true for the cases of models 2 and 3 with $C_\mu > 0.02$, which are characterized by much lower shedding frequencies.

3.2. Effects on alternate vortex shedding

In Fig. 7(a), instantaneous spanwise vorticity contours from the suction hole section are shown for model 2 with different suction momenta and a 90° (270°) suction angle. The PIV results (Chen et al., 2013(a)) are also attached to the numerical

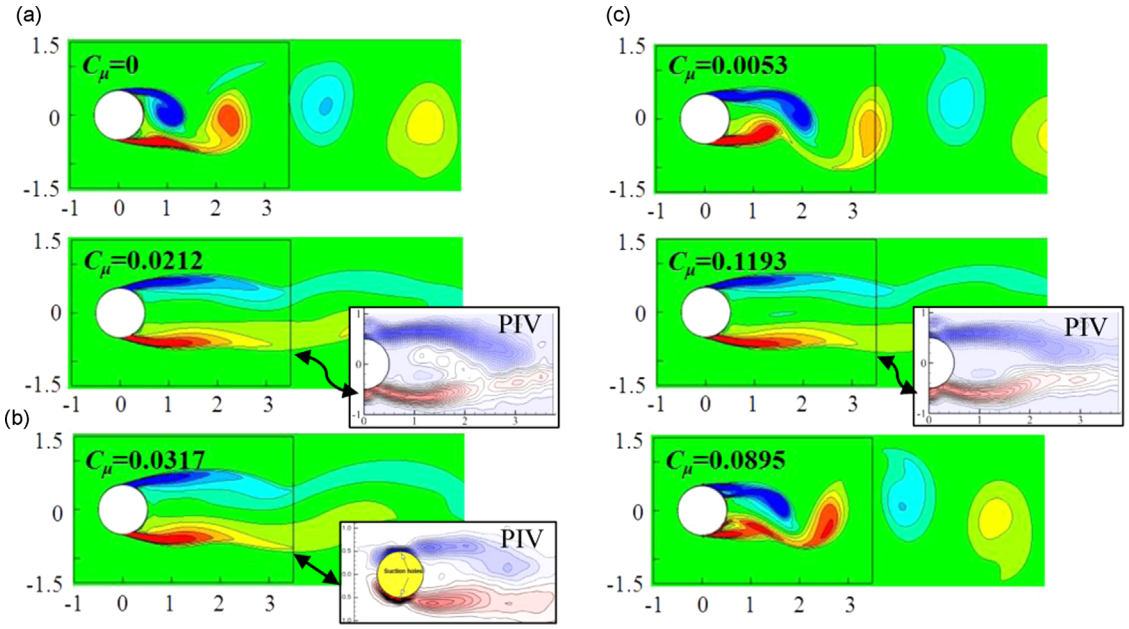

Fig. 7. Instantaneous span-wise vorticity distribution on suction holes section. (a) Model 2, (b) Model 3, (c) Model 1. It is noticed that the PIV results (Chen et al., 2013a, 2014) are also attached to the numerical cases with the same suction conditions in the (a) and (b), and the scales of numerical and experimental figures are the same.

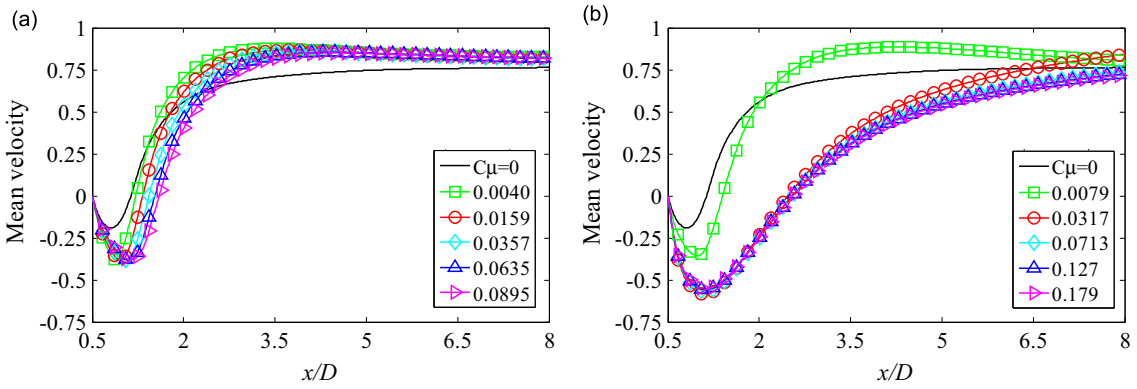

Fig. 8. Time-averaged stream-wise velocity distribution on mid-span section. (a) Model 1 and (b) Model 3.

cases with the same suction conditions, and the scales of the numerical and experimental figures are the same. For the uncontrolled or 20 L/min (i.e., $C_\mu=0.0053$) controlled cylinder, the wake is the strongly periodic vortex shedding pattern. When the suction rate increases from 40 L/min (i.e., $C_\mu=0.0212$) to 95 L/min (i.e., $C_\mu=0.119$), the periodic and concentrated Karman vortex shedding pattern is replaced by the symmetric and distributive vortex strip pair in the near wake. In the case of a sufficiently large suction rate of 40 L/min (i.e.,$C_\mu=0.0212$) for model 2, the shear layer on one side does not have enough energy to draw the opposite-sign shear layer on the other side in the absence of an increasing accumulation of vorticity on either side. This violates the precondition for alternate vortex shedding from a circular cylinder, according to the physical interpretation of vortex shedding proposed by Gerrard (1966) and Coutanceau et al. (1988). As expected, alternate vortex shedding in the near wake is suppressed by the steady suction method under certain arrangements and suction strengths of suction holes. They are in good agreement with the PIV measurements by Chen et al. (2013(a)) shown in Fig. 7(a), which suggests that the alternating vortex shedding changed to a symmetrical pattern in the near wake. As the suction flow rate varied from 40 to 95 L/min (i.e.,C_μ varying from 0.0317 to 0.179), the suppression of alternate vortex shedding is also achieved in model 3 as shown in Fig. 7(b). The phenomenon also agrees with the PIV measurements in the near wake (Chen et al., 2014). However, even when the suction rate is increased to 95 L/min (i.e.,$C_\mu=0.0895$), model 1 with its larger axial spacing is still not able to suppress the alternate vortex shedding, as shown in Fig. 7(c).

Fig. 8 shows the time-averaged streamwise velocity profiles in the downstream direction to evaluate the control effectiveness of the formation lengths of primary vortices. For model 1, the formation lengths are larger than the uncontrolled case and gradually increase with the suction flow rate. However, for model 3, the formation lengths are evidently divided into the case with $C_\mu=0.0079$ and the cases with $C_\mu\geq 0.0317$, where the cases in the latter category are very close to each other and much larger than the former. Such flow features in the wake are in agreement with the changes in the aerodynamic forces with changes in the spacing arrangements and suction flow rates. It is worth noting that model 2 behaves similarly to model 3 in terms of their velocity profiles. It also should be noted that more information about the variations along the span of both the time-averaged velocity and the velocity fluctuations in the near wake will be discussed in more detail in the Section 4.2.

4. Three-dimensional effects in the near wake

4.1. Strongly three-dimensional flow pattern

Summarizing the above results, one can divide the 90° angle cases into two distinct groups: One group comprises model 1 and model 2 with $C_\mu<0.0212$ and model 3 with $C_\mu<0.0317$. These cases cannot suppress alternate primary vortex shedding behind the circular cylinder and still have relatively high drag and lift reduction factors. The second group is characterized by effective control of the aerodynamic forces (i.e., the reduction of the lift fluctuation by 80%) and sufficient suppression of alternate vortex shedding, including model 2 with $C_\mu\geq 0.0212$ and model 3 with $C_\mu\geq 0.0317$. Their control effectiveness is very close to each other among the various cases in the latter group, which has been demonstrated by the similar reduction factors of the aerodynamic forces and the sufficient suppression of primary vortex shedding in the cross section perpendicular to the axis of the cylinder. Hereafter, the latter group is called the effective controlled cases.

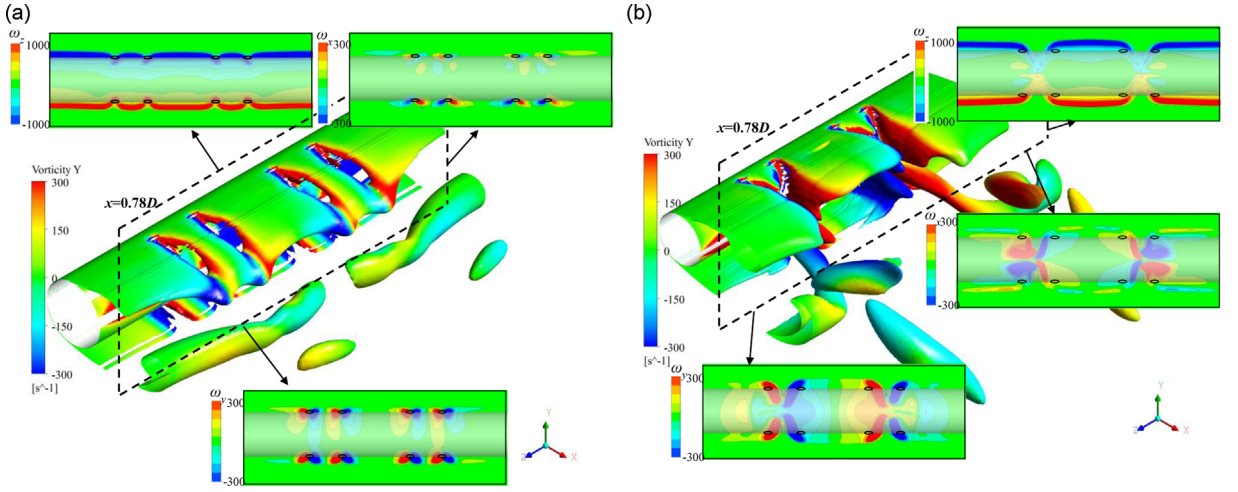

Fig. 9. Near wake flow divided into two patterns. (a) Pattern A, example from $C_\mu=0.0053$ of model 2, (b) Pattern B, example from $C_\mu=0.1193$ of model 2. The central three-dimensional structures are iso-surfaces of Q value, but colored by the cross-stream (y direction) voriticty component. The surrounding two-dimensional sliced sections are the contours of span-wise (ω_z), stream-wise (ω_x) and cross-stream (ω_y) vorticity components respectively on the same z–y section, specifically $x=0.78$ D.

Additionally, characterization of the strongly three-dimensional near wake (i.e., pattern B) will be introduced in the following section.

Corresponding to the two groups mentioned above, the near wake can be divided into two different patterns, i.e., pattern A and pattern B, corresponding to Fig. 9(a) and (b). The Q criterion proposed by Hunt et al. (1988) is employed to show the three-dimensional flow structures. The definition of Q is taken as $Q=-(1/2)(\|\mathbf{S}\|^2-\|\mathbf{\Omega}\|^2)$, where $\mathbf{S}$ and $\mathbf{\Omega}$ denote the strain and rotation tensor, respectively. The instantaneous three-dimensional flows in the central region of Fig. 9(a) and (b) are the iso-surfaces of Q values, colored by the vertical vorticity component (ω_y). Surrounding it, the contours of the spanwise (ω_z), streamwise (ω_x) and cross-stream (ω_y) vorticity components are illustrated based on the same z–y plane, specifically the plane when $x=0.78$ D located within the recirculation region. Pattern A (Fig. 9(a)) is actually the result of isolated steady suction holes independent of each other. In the suction hole section, the flow separation is delayed to a degree that depends on the suction flow rate. The delay of flow separation enhances the entrainment of the potential flow into the near-wake recirculation region and tends to narrow the recirculation width. The spanwise vorticity component (ω_z) distribution clearly demonstrates this phenomenon behind each suction hole. However, due to spatial "localization" of the delayed separation, a difference in the velocity flow occurs between the downstream region of the suction hole and the lower-velocity recirculation region beside it. A streamwise vortex pair and a cross-stream vortex pair will necessarily be produced on both sides of each independent suction hole. Hereafter, they are called a "three-dimensional vortex pair" based on the difference from the dominant two-dimensionality of the separated shear layer and Karman vortex. From the ω_x and ω_y distributions, these three-dimensional vortex pairs are located at a similar height to the two-dimensional separated shear layer. From the perspective of the spanwise configuration, the generated three-dimensional vortex pairs are generally independent of each other. As a result of pattern A, the primary vortex formation length increases somewhat, but the alternate vortex shedding cannot be completely suppressed, e.g., the wake flow for model 2 with $C_\mu=0.0053$ in Fig. 7(a).

On the other hand, pattern B (Fig. 9(b)) demonstrates a distinct three-dimensional flow. It is characterized by the generation of convergent flow between two neighboring suction hole sections and stronger three-dimensional vortex pairs besides that convergent flow. Herein, convergent flow refers to the entrainment-amplified potential flow behind the suction holes that travels toward the middle of the two neighboring suction hole sections and tilts toward the horizontal plane at the middle-height of the cylinder. Obviously, for pattern B, the three-dimensional vortex pair is based on each convergent flow. From the vorticity component contours, three-dimensional vortex pairs are located at the mid-height region of the cylinder. As a result of pattern B, a more violent three-dimensionality effect takes place, and the regular and alternate Karman vortex shedding is successfully suppressed. The three-dimensional flow in Fig. 9(b) is applicable to other flows of Pattern B including model 2 and model 3 with certain suction flow rates. Fig. 10 shows the three-dimensional flows of model 3 for the cases with suction flow rates of 40 L/min (minimum value for achieving effective control) and 95 L/min (maximum value for achieving effective control). They are found to be in a similar pattern to those of model 2 (e.g., Fig. 9(b)). Pattern B is universal for effective suppression of Karman vortex shedding behind circular cylinders, at least for the cases investigated in the present study.

Next, the transition from pattern A (Fig. 9(a)) to pattern B (Fig. 9(b)) under the same axial arrangement of suction holes is explained with model 2 as an example. It has been suggested that the main characteristic of pattern B, i.e., the convergent flow, is induced by the strong interaction between two neighboring three-dimensional vortex pairs, produced separately by two neighboring suction holes. The strength of the interaction is dependent on the axial distance between the two neighboring suction holes and the suction flow rate (which directly influences the strength of the three-dimensional vortex pairs). When the two conditions are satisfied, the interaction between the opposite rotating-direction streamwise vortices, generated separately by two neighboring suction holes, forces them closer in the spanwise direction and tends towards the horizontal plane when $y=0$. Simultaneously, the counter-rotating cross-stream vortices, concomitant with the streamwise vortices, are forced closer in the spanwise direction and tend toward the vertical plane when $x=0$. One result is the convergence of potential flow into the intermediate region of two suction hole sections and a tendency toward the horizontal

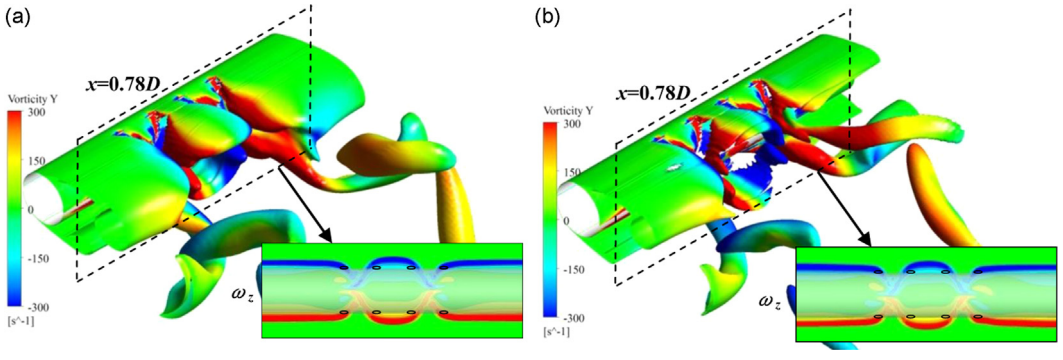

Fig. 10. Three-dimensional flows of pattern B for model 3. (a)$C_\mu=0.0317$, the minimum suction moment coefficient with effective control, (b)$C_\mu=0.1790$, the maximum suction moment coefficient with effective control. The information of quantities shown are the same as Fig. 9.

plane when $y=0$ and the vertical plane when $x=0$. In addition, a stronger three-dimensional vortex pair forms besides the convergent flow.

The strong three-dimensional effect of pattern B will be examined in more detail in the following subsections based on the spanwise variation of the flow field and the aerodynamic sectional forces. Conversely, the latter will verify the physical interpretation of the strongly three-dimensional effect of pattern B.

4.2. Variation of the flow field along the span

Fig. 11 shows the time-averaged velocity vector diagrams in the x–z planes of $y=0$, $D/6$, $D/3$ and $D/2$, respectively. These figures verify the generation of convergent flow and stronger cross-stream vortices besides the convergent flow for flow pattern B. It clearly shows that the higher-velocity potential flow converges into the intermediate section of the two neighboring suction hole sections, i.e., H1 and H2 or H3 and H4. Two clear cross-stream vortices (rotating around the y-axis) are formed on either side of each convergent flow in the x–z planes. The cross-stream vortices are visible over the entire vertical height range of the cylinder, which indicates larger-scale cross-stream vortices than those of pattern A. Between two convergent flows, a strong adverse flow towards the cylinder takes place, i.e., between the H2 and H3 suction hole section. It is worth noting that the cross-stream vortices and a strong adverse flow are also observed by PIV measurements (Chen et al., 2014).

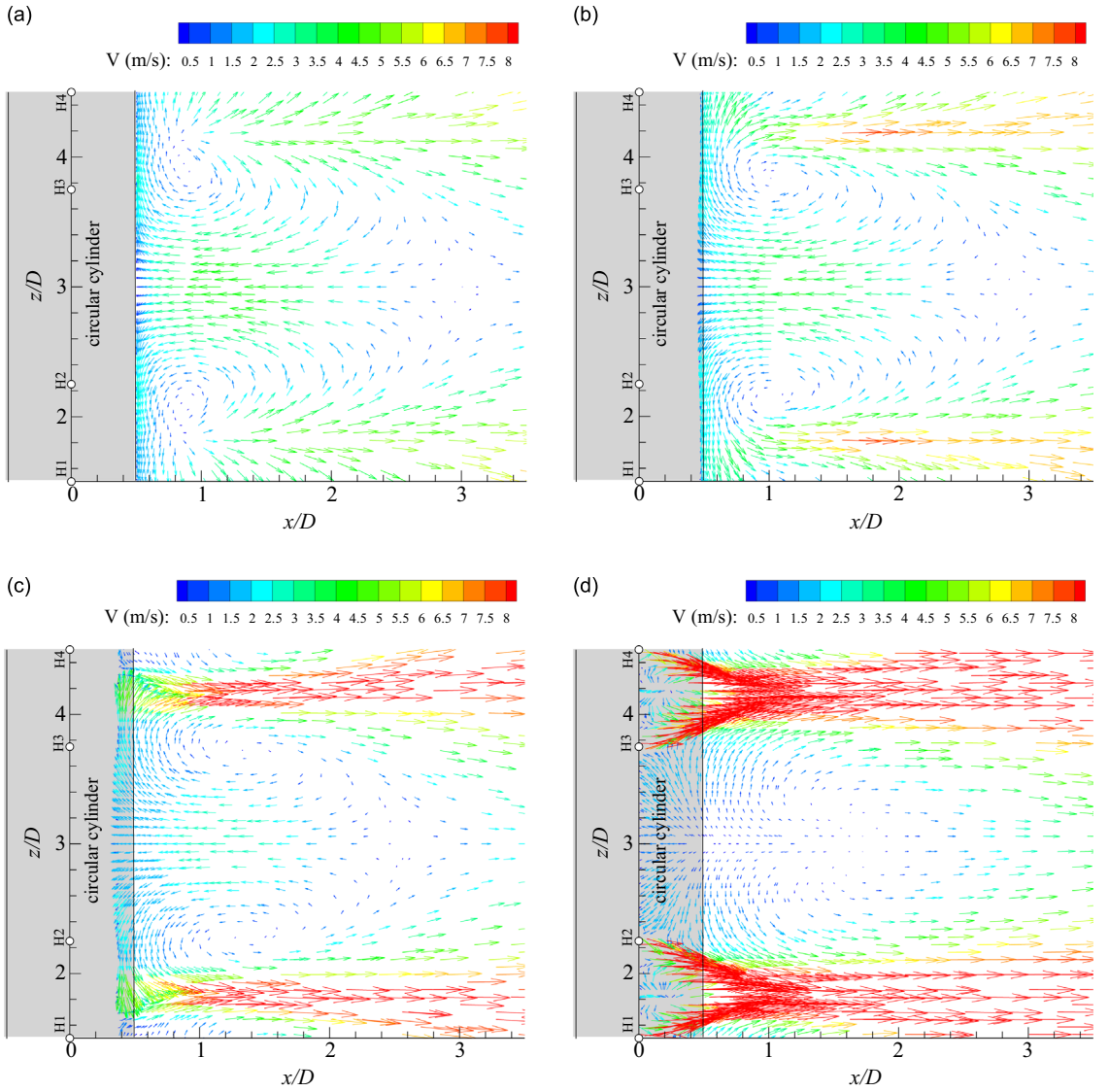

Fig. 11. Time-averaged velocity vector diagrams in the x–z planes, where the hollow circles on the z/D coordinate represent the suction holes of model 2, $C_\mu=0.0212$. (a)$y=0$. (b)$D/6$. (c)$D/3$. (d)$D/2$.

The distribution of turbulent kinetic energy is shown in Fig. 12, together with streamlines of time-averaged velocity. Fig. 12(a) shows a quantitative comparison between the uncontrolled case and model 2 with $C_\mu = 0.1193$ in the mid-span cross section, where experimental results (Chen et al., 2014) are also provided. The contour figures of numerical results and experimental results have the same scale but not the same legend range of the T.K.E. It can be concluded that the present numerical results agree qualitatively with the experimental results based on the common facts that the T.K.E. of pattern B is much smaller than that of the uncontrolled case and that the recirculation region of pattern B is much longer than that of the uncontrolled case. However, there is still quantitative disparity between the numerical and experimental effectively controlled cases. The T.K.E. of the effectively controlled case is smaller than that of the experimental result, and the length of the recirculation region in the effectively controlled case is approximately 0.5 D longer than that of the experimental result. The authors think that the quantitative difference between the numerical and experimental results possibly relies on the modeling characteristics of the random turbulent components inherently embedded in the SST (URANS) turbulence model. In the numerical situation, the time-averaged components and periodic components (related to Karman vortices) are directly solved while the random turbulent motions are erased to some extent due to modeling based on the eddy-viscosity hypothesis. Thus, the separated shear layers and the periodic Karman vortices in the near wake can be successfully

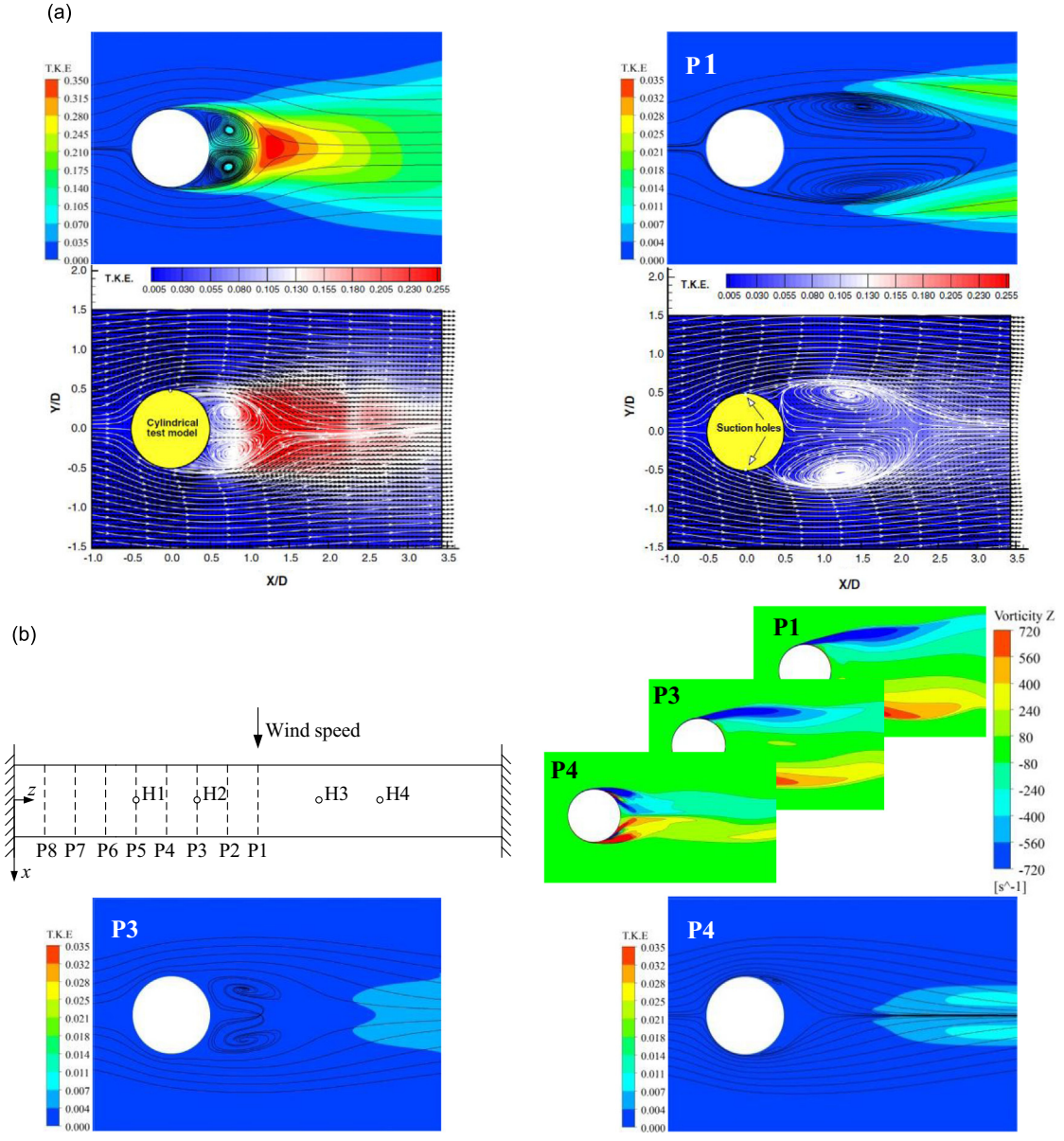

Fig. 12. (a) Comparison of streamlines of time-averaged velocity and distributions of turbulent kinetic energy between present numerical and experimental data by Chen et al. (2014); the left are uncontrolled cases while the right are effective controlled cases of mode 2 at $C_\mu = 0.1193$, at the mid-span cross section P1. (b) Comparison along the span, also including the instantaneous span-wise vorticity component.

controlled in both the numerical simulation and the experiment. The effects of three-dimensional random turbulent motions can be identified by comparing the experimental results with the URANS simulation results. The quantitative difference in the T.K.E. in the near wake (associated with the r.m.s. of the lift) as well as the slight difference in the instantaneous spanwise vorticity distribution in the far wake (shown in Fig. 7) demonstrate a common fact that the blending of random turbulent motions in the experiment promotes the fluctuations of shear layers far away from the cylinder, finally generating weak vortex shedding in the far wake. This is also the reason that the length of the recirculation region in the experiment is shorter than that in the numerical simulation in the presence of random turbulent motions. However, it is believed that the averaging-out of random turbulent fluctuations by URANS modeling will not influence the gross controlled flow configuration of pattern B significantly even at such high Reynolds numbers. The conceptual bases are that the separated shear layers are principally two-dimensional (Williamson, 1996) and remain laminar near the separation point; the suction holes are located at 90°, very close to the separation point; and the vigorous coherent Karman vortices dominate the near wake and are two-dimensional along the span on average even at such high *Re* (Szepessy, 1994). Thus, the two-dimensionality of the near wake even at such high *Re* opens the way to the achievement of the steady suction control method whose fundamental mechanism is to change it to strongly three-dimensional near wake.

For convenience, the various cross sections perpendicular to the axis of cylinder are named using P plus a number, as shown in Fig. 12(b), which will be employed hereafter, unless otherwise noted. The variation along the span of the instantaneous spanwise vorticity component, the distributions of the T.K.E., and the streamlines of the time-averaged velocity can be clearly seen in Fig. 12(b). In contrast, with the distribution of separated shear layers parallel to the oncoming flow direction in sections P1 and P3, a significantly narrowed recirculation region occurs in section P4, which is the result of convergent flow towards the horizontal plane when $y=0$ and the vertical plane when $x=0$. The small fluctuation in T.K.E. suggest that the averaged flow is similar to the instantaneous ones. Consequently, it seems reasonable to approximate the near-wake of pattern B as a semi-steady one.

4.3. Sectional aerodynamic characteristics

After analyzing the three-dimensional flow in the near wake, it is necessary to measure its effect on the sectional aerodynamic characteristics on the circular cylinder. Thus, the sectional drag coefficient ($C_{D'}$) and lift coefficient ($C_{L'}$) are introduced and estimated using the forces acting on a discretized cylinder surface with a finite spanwise distance l_c (herein, $l_c/D=0.075 \ll 1$), as defined below:

$$C_{D'} = \frac{D'}{\frac{1}{2}\rho U_\infty^2 l_c D} \tag{4}$$

$$C_{L'} = \frac{L'}{\frac{1}{2}\rho U_\infty^2 l_c D} \tag{5}$$

where D' and L' are the drag and lift, respectively, in terms of segment l_c.

Fig. 13 shows the spanwise distribution of the mean sectional drag coefficient (a) and the r.m.s. of the sectional lift coefficient (b) for three models. It should be noted that half of the spanwise length of cylinder is shown accounting for the symmetry about the mid-span center, where $z/D=0$ is the end boundary and $z/D=3$ is the mid-span center. In addition, the notation of suction holes mentioned in the following discussion is the same as in Fig. 12(b). Model 1 is typical for pattern A, and model 2 with $C_\mu=0.0212$ and model 3 with $C_\mu=0.0317$ are typical for pattern B. For pattern A, only the sectional drag and lift coefficients near the localized suction holes are smaller than in the other sections because of the delay of flow separation behind the suction holes, together with the independence of the localized flow behind each suction hole. On the other hand, for pattern B, the sectional drag coefficients between H2 and H3 (located in the other half of the spanwise

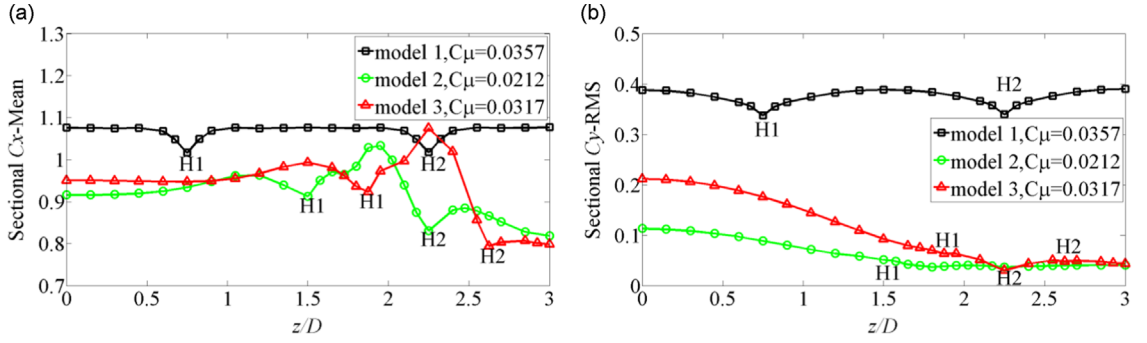

Fig. 13. Spanwise distribution of (a) the mean sectional drag coefficient and (b) r.m.s of sectional lift coefficient. Model 1 with $C_\mu=0.0357$ is typical for patter A. Model 2 with $C_\mu=0.0212$ and model 3 with $C_\mu=0.0317$ are typical for pattern B; $z/D=0$ is the end boundary and $z/D=3$ is the mid-span center; H1 and H2 are the suction holes.

length) are much lower, which plays a key role in reducing the total drag forces. Surprisingly, the values between H1 and H2 reach the peak level. In contrast to the sectional drag coefficients, not only the range between H2 and H3 but also the sectional lift coefficients between H1 and H2 remain at low values. The decrease in the fluctuating sectional lift coefficients between H1 and H4 can be explained by the semi-steady near-wake flow of pattern B.

Fig. 14(a)–(d) shows the distributions with angle θ of the mean pressure and fluctuating pressure coefficients for the mid-span section. The characteristics of the pressure distributions roughly coincide with those of the force coefficients discussed in Section 3.1. Specifically speaking, model 1 has a gradually changing tendency against suction momenta, whereas the pressure curves overlap each other when $C_\mu = 0.0212 \sim 0.119$ for model 2 and $C_\mu = 0.0317 \sim 0.179$ for model 3. The latter phenomenon is attributed to the universality of pattern B. It is noticed that only model 2 is shown here due to space constraints. Fig. 14(e) shows the time-averaged pressure distributions at different cross sections for pattern B, taking model 2 with $C_\mu = 0.0212$ as an example. The hump-shape at approximately 180° of P1 and P2 results from the high-velocity reverse flow towards the rear of the cylinder. It induces a small mean sectional drag within the mid-span region (i.e., between H2 and H3). However, for the P4 section, the lower pressure regions at approximately 120° and 240° (marked by

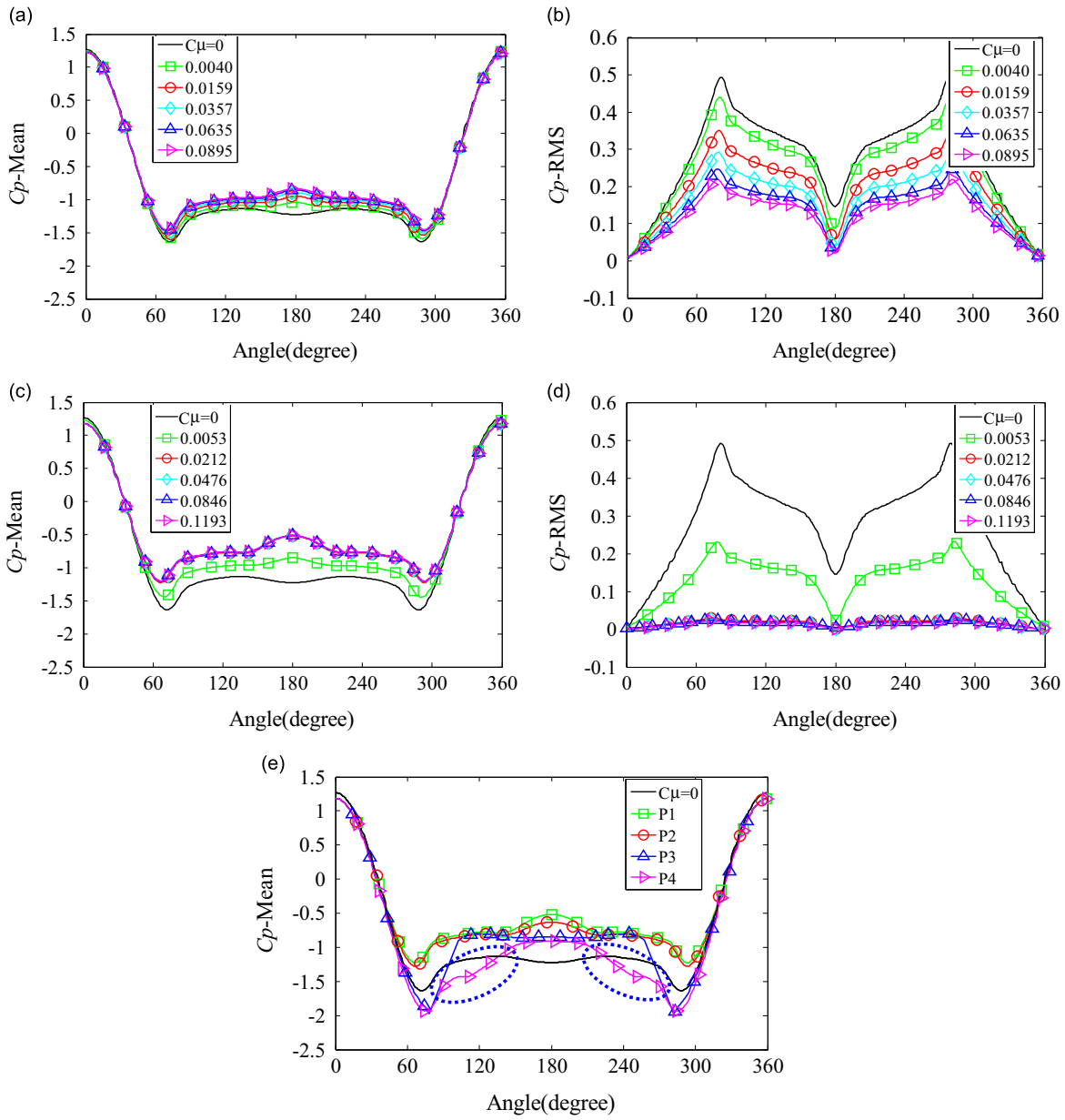

Fig. 14. Pressure distribution with azimuthal angle of (a) and (b) model 1 and (c) and (d) model 2 at the mid-span section. The left is the mean pressure coefficients while the right is the fluctuating pressure coefficients, (e) Distribution of fluctuating pressure at different cross sections for model 2 with $C_\mu = 0.0212$ (For interpretation of the references to color in this figure,the reader is referred to the web version of this article).

the green ellipses in Fig. 14(e)) means that the negative-pressure shear layers separate very close to the wall of cylinder when the convergent flow happens. Ultimately, it results in a peak value of the mean sectional drag coefficient between H1 and H2, which contributes to larger force reduction factors (i.e., lower control effectiveness) of the total integrated drag than of the total lift.

4.4. Axial spacing of the suction holes to generate pattern B

The axial spacing of the suction holes is more critical than the suction flow rate, as indicated by the phenomenon that model 1 cannot reach pattern B even when the suction flow rate is more than two times that of models 2 and 3. As discussed in Section 4.1, the convergent flow between two neighboring suction holes is the key to produce the strong three-dimensionality effect and thereby control the aerodynamic forces effectively. In some sense, the convergent flow of pattern B between two original suction holes plays the role of "a larger suction hole". Model 2 and model 3 have the same minimal axial spacing, and the near wake convergent flow behaves similarly under a certain suction flow rate. Thus, it seems arguable that the minimal axial spacing would be the critical length scale determining whether strongly three-dimensional flow takes place. The upper limit of axial spacing is suggested to be between 0.75 D (the minimal spacing of model 2 and model 3) and 1.5 D (the minimal spacing of model 1). Furthermore, the axial distance between two convergent flows (or two neighboring "larger suction holes") is also suggested to have an upper limit to maintaining effective suppression of alternate vortex shedding within this axial range. Thus, more cases are needed to determine the upper limits of both the axial spacing between two isolated suction holes to generate the convergent flow and the axial distance between two convergent flows to maintain the suppression of alternate vortex shedding.

5. Conclusions

The control effectiveness of the steady suction method on a stationary circular cylinder with several isolated suction holes on the surface was investigated numerically. An effective combination of azimuthal position, axial spacing and suction flow rate of the suction holes was determined to significantly reduce the fluctuating lift force acting on the circular cylinder and suppress the alternate vortex shedding in the near wake.

First, the azimuthal location of the suction holes is found to be vital. Among all tested azimuthal positions, the positions (θ=90° and 270°) close to the separation point are optimal to decrease the aerodynamic forces on the cylinder for all three models. Restricting to the most effective azimuthal angles (θ=90° and 270°), both the axial spacing between two neighboring suction holes and the suction flow rate determine the control effectiveness. For model 1 (with minimum spacing 1.5 D), the increase in the suction momentum coefficient C_μ (ranging from 0 to 0.0895) gradually results in the reduction of the mean drag and r.m.s. of lift. However, the performances of models 2 and 3 (with minimal spacing of 0.75 D) are remarkably different from that of model 1. When C_μ exceeds 0.0212 for model 2 and 0.0317 for model 3, much more effective control of aerodynamic forces (i.e., reduction of lift fluctuation by 80%) and the successful suppression of alternate vortex shedding in the near wake can be achieved, but a further increase in suction strength has no or little influence on the control effectiveness.

Next, an explanation of the cause of effective control was provided based on the three-dimensional near-wake flow. It was discovered that the near wake can be divided into two different patterns: pattern A and pattern B. Pattern A is the result of independent controlled flows by each isolated suction hole, inducing the preservation of alternate vortex shedding in the wake. However, effective aerodynamic control is closely related to obvious three-dimensionality phenomenon in the near wake, i.e., pattern B. Pattern B is characterized by the generation of convergent flow between two neighboring suction hole sections and stronger, larger-scale three-dimensional vortex pairs adjacent to that convergent flow. In terms of the side-view section, pattern B successfully suppresses the regular and alternate vortex shedding. The transition from pattern A to pattern B is suggested to be induced by the strong interaction between two neighboring but counter-rotating three-dimensional vortices produced separately by two neighboring suction holes. The effects of flow pattern B on the variation of the flow field and sectional aerodynamic forces or pressure in different cross sections are investigated in detail. Pattern B has very low turbulent kinetic energy in the near wake in different cross sections, resulting in low fluctuation of the sectional lift. The convergent flow between two neighboring suction holes increases the sectional drag because of the negative-pressure shear layers separating close to the wall of the cylinder. In contrast, the high-velocity adverse flow towards to the rear of the cylinder decreases the sectional drag between two convergent flows, which leads to the lower control effectiveness of the total drag coefficient compared with the total lift coefficient.

Finally, the parameters required to achieve effective control (i.e., to generate pattern B) have been discussed. The upper limit of the axial spacing between two neighboring suction holes to form pattern B is suggested to be between 0.75 D and 1.5 D when the suction momentum exceeds a certain value.

Acknowledgments

This research was funded by the National Natural Science Foundation of China (NSFC) (51378153, 51008093, 51161120359 and 91215302) and the Ministry of Transport of the People's Republic of China (2011318494180).

References

Amitay, M., Smith, B.L., Glezer, A., 1998. Aerodynamic flow control using synthetic jet technology. AIAA, 98–0208.
ANSYS CFX 14.0[Computer softerware], Canonsburg, PA, Ansys.2011.
Bearman, P., Branković, M., 2004. Experimental studies of passive control of vortex-induced vibration. European Journal of Mechanics-B/Fluids 23 (1), 9–15.
Braza, M., Perrin, R., Hoarau, Y., 2006. Turbulence properties in the cylinder wake at high Reynolds numbers. Journal of Fluids and Structures 22.6, 757–771.
Chen, W.L., Hu, H., Li, H., 2013(a). Suppression of vortex shedding from a circular cylinder by using a suction flow control method. AIAA Paper 2013–0103, In: Proceedings of the 51st AIAA Aerospace Sciences Meeting including the New Horizons Forum and Aerospace Exposition, Grapevine (Dallas/Ft. Worth Region), Texas.
Chen, W.L., Xin, D.B., Xu, F., Li, H., Ou, J.P., Hu, H., 2013. Suppression of vortex-induced vibration of a circular cylinder using suction-based flow control. Journal of Fluids and Structures 42, 25–39.
Chen, W.L., Hu, H., Li, H., 2014. An experimental study on a suction flow control method to reduce the unsteadiness of the wind loads acting on a circular cylinder. Experiments in Fluids 55 (4), 1–20. 1707.
Chng, T.L., Rachman, A., Tsai, H.M., Zha, G.C., 2009. Flow control of an airfoil via injection and suction. Journal of Aircraft 46 (1), 291–2300.
Coutanceau, M., Boyce, P., Guerineau, G., 1988. The effect of high-order separations on the onset of secondary instability in the wake boundary of a circular cylinder. Academie des Sciences Paris Comptes Rendus Serie Sciences Mathematiques 306, 1259–1263.
Feng, L.H., Wang, J.J., Pan, C., 2010. Effect of novel synthetic jet on wake vortex shedding modes of a circular cylinder. Journal of Fluids and Structures 26 (6), 900–917.
Feng, L.H., Wang, J.J., 2012. Synthetic jet control of separation in the flow over a circular cylinder. Experiments in fluids 53 (2), 467–480.
Fransson, J.H., Konieczny, P., Alfredsson, P.H., 2004. Flow around a porous cylinder subject to continuous suction or blowing. Journal of Fluids and Structures 19 (8), 1031–1048.
Gerrard, J.H., 1966. The mechanics of the formation region of vortices behind bluff bodies. Journal of Fluid Mechanics 25 (02), 401–413.
Glezer, A., Amitay, M., 2002. Synthetic jets. Annual Review of Fluid Mechanics 34 (1), 503–529.
Greenblatt, D., Paschal, K.B., Yao, C.S., Harris, J., Schaeffler, N.W., Washburn, A.E., 2006. Experimental investigation of separation control part 1: baseline and steady suction. AIAA Journal 44 (12), 2820–2830.
Hunt, J.C., Wray, A.A., Moin, P., 1988. Eddies, streams, and convergence zones in turbulent flows. Center for Turbulence Research Report, Stanford193–208 CTR-S88.
Menter, F.R., 1994. Two-equation eddy-viscosity turbulence models for engineering applications. AIAA Journal 32 (8), 1598–1605.
Menter, F.R., Kuntz, M., Langtry, R., 2003. Ten years of industrial experience with the SST turbulence model. Turbulence Heat and Mass transfer 4 (1).
Norberg, C., 1994. An experimental investigation of the flow around a circular cylinder: influence of aspect ratio. Journal of Fluid Mechanics 258, 287–316.
Owen, J.C., Bearman, P.W., Szewczyk, A.A., 2001. Passive control of VIV with drag reduction. Journal of Fluids and Structures 15 (3), 597–5605.
Qin, N., Zhu, Y., Poll, D.I.A., 1998. Surface suction on aerofoil aerodynamic characteristics at transonic speeds. Proceedings of the institution of mechanical engineers. Part G: Journal of Aerospace Engineering 212 (5), 339–351.
Roshko, A., 1993. Perspectives on bluff body aerodynamics. Journal of Wind Engineering and Industrial Aerodynamics 49 (1), 79–100.
Seal, C.V., Smith, C.R., 1999. The control of turbulent end-wall boundary layers using surface suction. Experiments in Fluids 27 (6), 484–4496.
Shiels, D., Leonard, A., 2001. Investigation of a drag reduction on a circular cylinder in rotary oscillation. Journal of Fluid Mechanics 431 (1), 297–322.
Szepessy, S., Bearman, P.W., 1992. Aspect ratio and end plate effects on vortex shedding from a circular cylinder. Journal of Fluid Mechanics 234, 191–217.
Szepessy, S., 1994. On the spanwise correlation of vortex shedding from a circular cylinder at high subcritical Reynolds number. Physics of Fluids 6 (7), 2406–22416.
Tokumaru, P.T., Dimotakis, P.E., 1991. Rotary oscillation control of a cylinder wake. Journal of Fluid Mechanics 224, 77–90.
West, G.S., Apelt, C.J., 1982. The effects of tunnel blockage and aspect ratio on the mean flow past a circular cylinder with Reynolds numbers between 104 and 105. Journal of Fluid Mechanics 114, 361–377.
Wilcox, D.C., 1988. Reassessment of the scale-determining equation for advanced turbulence models. AIAA Journal 26 (11), 1299–1310.
Williamson, C.H.K., 1996. Vortex dynamics in the cylinder wake. Annual Review of Fluid Mechanics 28, 477–539.
Wu, C.J., Wang, L., Wu, J.Z., 2007. Suppression of the von Kármán vortex street behind a circular cylinder by a travelling wave generated by a flexible surface. Journal of Fluid Mechanics 574, 365–392.
Zuo, D., Jones, N.P., Main, J.A., 2008. Field observation of vortex-and rain–wind-induced stay-cable vibrations in a three-dimensional environment. Journal of Wind Engineering and Industrial Aerodynamics 96 (6), 1124–1133.
Zuo, D., Jones, N.P., 2010. Interpretation of field observations of wind-and rain-wind-induced stay cable vibrations. Journal of Wind Engineering and Industrial Aerodynamics 98 (2), 73–87.